Guiding and polarization shaping of vector beams in anisotropic media

Nilamoni Daloi,[1] Pardeep Kumar,[2] and Tarak Nath Dey[1,*]
[1]*Department of Physics, Indian Institute of Technology Guwahati, Guwahati 781039, Assam, India*
[2]*Max Planck Institute for the Science of Light, Staudtstrasse 2, 91058 Erlangen, Germany*

(Received 28 April 2022; revised 25 May 2022; accepted 1 June 2022; published 21 June 2022)

We investigate a scheme to guide a weak vector beam using optically written waveguides inside atomic vapor, while controlling its polarization rotation. The atoms are prepared in the four-level tripod configuration in the presence of an external magnetic field. The three transitions of the tripod system are driven by a strong control beam and the two orthogonal polarization components of a weak vector beam (VB). A suitable spatial intensity profile and the detuning of the control field facilitate the generation of an optical fiberlike refractive index gradient across the atomic vapor. This enables waveguiding of the weak VB for a couple of Rayleigh lengths. Further, the magnetic-field-induced anisotropy of the tripod system creates a difference in the refractive indices of its two components. This is the reason behind the polarization shaping of VB. The mechanism of efficient guiding of VB with controllable polarization may have important applications in high-density optical communication and quantum information.

DOI: 10.1103/PhysRevA.105.063714

I. INTRODUCTION

Vector beams (VBs) also known as fully structure light (FSL) beams have a great advantage over their scalar counterparts, due to their spatially inhomogeneous polarization distribution. Coherent control of polarization, phase, and amplitude gives us complete freedom to manipulate FSL. A vector superposition of two orthogonally polarized components can produce a VB or FSL beam [1–3]. The constituent of VB carries orbital angular momentum (OAM) with Laguerre-Gaussian (LG) modes [4]. Two LG modes with equal and opposite OAM can generate a cylindrical vector (CV) beam that carries a net-zero OAM. The polarization distribution of CV beam is found to be radial, azimuthal, and spiral with respect to the axial symmetry of the beam. On the other hand, a full Poincaré (FP) [2] beam has a transverse polarization distribution that varies both in the azimuthal and radial directions. The FP beam bears a nonzero OAM value, which is in contrast to the CV beam. Based on the transverse inhomogeneity of polarization, the FP can be classified as lemon, star, and web VBs.

The acclamation of VBs comes from their applicability in myriads of areas as well as developments in their generation methods. With the use of a high numerical aperture (NA) lens, CV beams can create a spot size as small as $0.1612\lambda^2$ [5]. This realization is possible due to the existence of a strong longitudinal polarization component [6]. The focusing property of CV beams has applications in single-molecule spectroscopy, STED [7], confocal microscopy [8–10], efficient laser cutting [11], and optical trapping of particles [12,13]. The inhomogeneous polarization distribution of VBs has application in polarization dependent measurements [14]. In quantum information, a high-dimensional Hilbert space [15] can be facilitated by the VBs that employ their polarization inhomogeneity and OAM. This high-dimensional Hilbert space can be leveraged to encode single-photon qubits [16]. In optical communication, the transverse polarization distribution of vector modes can be used to increase the transmission data rate of free space optical communication [17]. The spatial degree of freedom of scalar OAM carrying beams has been used to increase information content [18] in optical communication. The diffraction of these OAM beams during propagation can be mitigated by using a Kerr medium [19]. Although, OAM beams suffer from fragmentation into multiple spatial solitons during nonlinear propagation [20,21], this fragmentation can be inhibited by using VBs instead of scalar beams [22–24]. CV beams can propagate in a saturable Kerr nonlinear medium for longer distances compared to scalar beams [25] without undergoing significant changes to their transverse spatial intensity profile. It is important to maintain minimum absorption and controllable diffraction for VB, which is an essential criterion for many of the aforementioned applications. In addition, exploiting the polarization structure opens up a completely new degree of freedom for manipulation of FSL [26].

In this work, we propose a VB guiding scheme based on optically written waveguides in atomic vapor [27,28]. The three transitions of the tripod system are driven by a strong control field and the two orthogonal polarization components of a probe VB. The strong control field facilitates absorptionless VB propagation through electromagnetically induced transparency (EIT). An external longitudinal magnetic field is employed to induce anisotropy, which creates a difference in the refractive indices of the two orthogonally polarized VB components. This difference in refractive index varies with the magnetic field strength and, in turn, enables VB polarization rotation control during propagation. Furthermore,

*tarak.dey@iitg.ac.in

a control field with a suitable spatial intensity profile and detuning can create a "core-cladding" type refractive index gradient, providing diffractionless VB propagation for several Rayleigh lengths. The degree of waveguiding can be dynamically controlled via the magnetic field and control field detuning. There has been work related to vector beam guiding using anisotropic crystals [29] and generation of diffractionless vector Bessel beams with axicons [30]. Compared to these methods, an atomic medium provides dynamic control of the relevant parameters, which is not possible with crystals due to their fixed optical properties.

The paper is organized as follows. Section I contains a brief introduction on vector beam, its applications, and the findings of our work. Section II contains the theoretical formalism used in the work. Section III collates the results of this paper with explanations. Finally, Sec. IV contains the conclusion of the paper.

II. THEORETICAL FORMULATION

A. Level system

Engineering of spatial refractive index in the transverse plane is the key feature for diffraction-free propagation of the vector beam through the medium. A suitable modulation of spatial refractive index by the application of the spatial dependent control field enables waveguidelike structure inside the medium. In addition, the rotation of the polarization angle in the transverse plane of the VB is essentially dependent on the difference in refractive indices of its two components. This variation can be adjusted by a magnetic field. Hence the manipulation of the spatial refractive index makes it possible to achieve an efficient control over diffraction as well as polarization rotation of VB while it is propagating through the medium. In this regard, a four-level tripod system as shown in Fig. 1 is a natural candidate for the fulfillment of the above criteria without absorption. In Fig. 1, a longitudinal magnetic field can be used to remove the degeneracy among the states $|1\rangle$, $|0\rangle$, and $|2\rangle$. The energy of $|0\rangle$ is set to be zero and $|4\rangle$ is taken as the excited state. The states $|3\rangle$ and $|4\rangle$ are coupled by a strong control field, $\vec{E}_c$, which is defined as

$$\vec{E}_c(r,t) = \hat{e}_c \mathcal{E}_c(r) e^{-i(\omega_c t - k_c z)} + \text{c.c.}, \tag{1}$$

where $\mathcal{E}_c$, $\hat{e}_c$, ω_c, and k_c are the slowly varying envelope, the polarization, the frequency, and the wave vector of the control field, respectively. A weak $\hat{x}$-polarized probe field of frequency ω_p and propagation constant k_p can be decomposed in terms of two orthogonal polarization basis $\hat{\sigma}_i$, $(i \in R, L)$,

$$\vec{E}_p(r,t) = \hat{x}\mathcal{E}_p(\vec{r}) e^{-i(\omega_p t - k_p z)} + \text{c.c.} \tag{2a}$$

$$= \sum_{i=R,L} \hat{\sigma}_i \mathcal{E}_i(\vec{r}) e^{-i(\omega_p t - k_p z)} + \text{c.c.}, \tag{2b}$$

where the right (left) circularly polarized component $\mathcal{E}_R$ ($\mathcal{E}_L$) couples $|1\rangle \leftrightarrow |4\rangle$ ($|2\rangle \leftrightarrow |4\rangle$) transition. The level configuration in Fig. 1 can be realized with rubidium (Rb) atomic vapor in the presence of a magnetic field. We choose the Zeeman sublevels of ^{87}Rb D_2 ($5^2S_{1/2} \rightarrow 5^2P_{3/2}$) transition hyperfine structure as $|1\rangle = |5^2S_{1/2}, F = 1, m_F = -1\rangle$, $|2\rangle = |5^2S_{1/2}, F = 1, m_F = +1\rangle$, which makes $|0\rangle = |5^2S_{1/2}, F = 1, m_F = 0\rangle$. States $|3\rangle$ and $|4\rangle$ can be taken as $|3\rangle = |5^2S_{1/2}, F = 2, m_F = 1\rangle$ and $|4\rangle = |5^2P_{3/2}, F = 0, m_F = 0\rangle$. The time-dependent Hamiltonian of the system as shown in Fig. 1 can be expressed under the electric dipole approximation as

$$\boldsymbol{H} = \boldsymbol{H}_0 + \boldsymbol{H}_B + \boldsymbol{H}_I, \tag{3a}$$

$$\boldsymbol{H}_0 = \hbar(\omega_{40}|4\rangle\langle 4| + \omega_{30}|3\rangle\langle 3|), \tag{3b}$$

$$\begin{aligned}\boldsymbol{H}_I &= -\hat{d}\cdot\vec{E} \\ &= -[\vec{\boldsymbol{d}}_{41}\cdot(\hat{\sigma}_R\mathcal{E}_R e^{-i\omega_p t} + \text{c.c.})|4\rangle\langle 1| \\ &\quad + \vec{\boldsymbol{d}}_{42}\cdot(\hat{\sigma}_L\mathcal{E}_L e^{-i\omega_p t} + \text{c.c.})|4\rangle\langle 2| \\ &\quad + \vec{\boldsymbol{d}}_{43}\cdot(\hat{e}_c\mathcal{E}_R e^{-i\omega_c t} + \text{c.c.})|4\rangle\langle 3|] + \text{H.c.},\end{aligned} \tag{3c}$$

where ω_{j0} $(j = 4, 3)$ is the frequency separation between state $|j\rangle$ and ground state $|0\rangle$ and $\vec{\boldsymbol{d}}_{4i} = \langle 4|\hat{\boldsymbol{d}}|i\rangle$ $(i = 1, 2, 3)$ are matrix elements of the dipole moment operator $\hat{\boldsymbol{d}}$, representing the induced dipole moments, corresponding to $|i\rangle \leftrightarrow |4\rangle$ transition. The magnitude of Zeeman shift between the ground-state levels is given by $\beta_L = g_F\mu_B B/\hbar$, where g_F and μ_B are the Landé g factor and Bohr magneton, respectively. To remove explicit time dependency in the Hamiltonian H, we use the following unitary transformation:

$$\hat{U} = e^{-i\omega_p t|4\rangle\langle 4| - i(\omega_p - \omega_c)t|3\rangle\langle 3|}. \tag{4}$$

The effective Hamiltonian obeying the Schrödinger equation in the transformed basis is given as $\mathcal{H} = \hat{U}^\dagger H\hat{U} - i\hbar\hat{U}^\dagger\partial_t\hat{U}$, which under rotating wave approximation gives

$$\begin{aligned}\frac{\mathcal{H}}{\hbar} &= -[(\delta_p - \delta_c)|3\rangle\langle 3| + \delta_p|4\rangle\langle 4|] + \hbar\beta_L(|2\rangle\langle 2| - |1\rangle\langle 1|) \\ &\quad - \hbar[\Omega_R|4\rangle\langle 1| + \Omega_L|4\rangle\langle 2| + \Omega_c|4\rangle\langle 3|] + \text{H.c.}\end{aligned} \tag{5}$$

In Eq. (5), the one photon probe detuning is $\delta_p = \omega_p - \omega_{40}$ and Rabi frequencies for the probe field components are

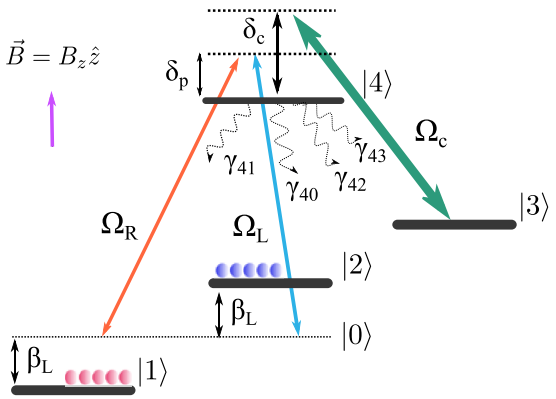

FIG. 1. Schematic diagram of a four-level tripod system. A magnetic field, $\vec{B} = B_z\hat{z}$, generates the Zeeman sublevels, $|1\rangle$, $|0\rangle$, and $|2\rangle$, with an energy separation of $\hbar\beta_L$ between them. The energy of $|0\rangle$ is indiscriminately set to zero and $|4\rangle$ is taken as the excited state. The right circularly polarized component, $\vec{E}_R$, and the left circularly polarized component, $\vec{E}_L$, of a weak probe VB drives the transitions, $|1\rangle \leftrightarrow |4\rangle$ and $|2\rangle \leftrightarrow |4\rangle$, respectively. The transition, $|3\rangle \leftrightarrow |4\rangle$, is coupled by a strong control field, $\vec{E}_c$. The spontaneous emission decay rate from $|4\rangle$ to $|j\rangle$ $(j = 0, 1, 2, 3)$ is denoted by γ_{4j}. The detunings of the probe and control fields are denoted by δ_p and δ_c, respectively.

defined as

$$\Omega_R = \frac{\vec{\boldsymbol{d}}_{41}\cdot\hat{\sigma}_R}{\hbar}\mathcal{E}_R, \quad \Omega_L = \frac{\vec{\boldsymbol{d}}_{42}\cdot\hat{\sigma}_L}{\hbar}\mathcal{E}_L. \tag{6}$$

The detuning and Rabi frequency of control is denoted as

$$\delta_c = \omega_c - \omega_{43}, \quad \Omega_c = \frac{\vec{\boldsymbol{d}}_{43}\cdot\hat{e}_c\mathcal{E}_c}{\hbar}. \tag{7}$$

The dynamics of atomic state populations and coherences are governed by the following Liouville equation:

$$\frac{\partial\rho}{\partial t} = -\frac{i}{\hbar}[\mathcal{H},\rho] + \mathcal{L}_\rho. \tag{8}$$

In the above equation, the Liouville operator, $\mathcal{L}_\rho$, describes all incoherent processes and can be expressed as

$$\mathcal{L}_\rho = -\sum_{j=1}^{3}\frac{\gamma_{4j}}{2}(|4\rangle\langle 4|\rho - 2|j\rangle\langle j|\rho_{44} + \rho|4\rangle\langle 4|), \tag{9}$$

where γ_{4j} represents the radiative decay rates from the excited state, $|4\rangle$, to ground states, $|j\rangle$. The relevant equations of motion for atomic state populations and coherences of the four-level tripod system are then given by

$$\dot{\rho}_{44} = -\sum_{i=0}^{3}\gamma_{4i}\rho_{44} + i(\rho_{34}\Omega_c - \rho_{43}\Omega_c^* + \rho_{14}\Omega_R - \rho_{41}\Omega_R^* + \rho_{24}\Omega_L - \rho_{42}\Omega_L^*), \tag{10a}$$

$$\dot{\rho}_{41} = i\Delta_{14}\rho_{41} + i[\rho_{31}\Omega_c + \rho_{21}\Omega_L + (\rho_{11}-\rho_{44})\Omega_R], \tag{10b}$$

$$\dot{\rho}_{42} = i\Delta_{24}\rho_{42} + i[\rho_{32}\Omega_c + \rho_{12}\Omega_R + (\rho_{22}-\rho_{44})\Omega_L], \tag{10c}$$

$$\dot{\rho}_{43} = i\Delta_{34}\rho_{43} + i[\rho_{13}\Omega_R + \rho_{23}\Omega_L + (\rho_{33}-\rho_{44})\Omega_c], \tag{10d}$$

$$\dot{\rho}_{11} = \gamma_{41}\rho_{44} + i(\rho_{41}\Omega_R^* - \rho_{14}\Omega_R), \tag{10e}$$

$$\dot{\rho}_{12} = i\Delta_{12}\rho_{12} + i(\rho_{42}\Omega_R^* - \rho_{14}\Omega_L), \tag{10f}$$

$$\dot{\rho}_{13} = i\Delta_{13}\rho_{13} + i(\rho_{43}\Omega_R^* - \rho_{14}\Omega_c), \tag{10g}$$

$$\dot{\rho}_{22} = \gamma_{42}\rho_{44} + i(\rho_{42}\Omega_L^* - \rho_{24}\Omega_L), \tag{10h}$$

$$\dot{\rho}_{23} = i\Delta_{23}\rho_{23} + i(\rho_{43}\Omega_L^* - \rho_{24}\Omega_c), \tag{10i}$$

$$\dot{\rho}_{33} = \gamma_{43}\rho_{44} + i(\rho_{43}\Omega_c^* - \rho_{34}\Omega_c), \tag{10j}$$

$$\rho_{ij} = \rho_{ji}^*, \quad \sum_{i=1}^{4}\rho_{ii} = 1. \tag{10k}$$

In Eq. (10), $\Delta_{14} = \delta_p - \beta_L + i\Gamma_{14}$, $\Delta_{24} = \delta_p + \beta_L + i\Gamma_{34}$, $\Delta_{34} = \delta_c + i\Gamma_{24}$, $\Delta_{12} = 2\beta_L + i\Gamma_{12}$, $\Delta_{13} = \delta_c - \delta_p + \beta_L + i\Gamma_{13}$, and $\Delta_{13} = \delta_c - \delta_p - \beta_L + i\Gamma_{23}$. Here, Γ_{ij} and Γ_{i4} are the decoherence rate of ρ_{ij} and ρ_{i4}, respectively. For simplicity, we assume $\gamma_{4i} = \gamma$ $(i < j;\ i, j \in 0, 1, 2, 3)$.

B. Refractive index of the medium

A minimum absorption is a prerequisite for VB propagation through the medium. Otherwise, huge absorption can degrade both envelope shape as well as transmission of VB. A strong control field-assisted EIT can make an otherwise opaque medium transparent for a weak probe field. The intensity of the probe field ensures that the perturbation analysis of the system retains the two lowest-order contributions while neglecting the higher orders in the expansion under steady-state conditions. Under the assumption of $|\mathcal{E}_c| \gg |\mathcal{E}_{R,L}|$, $\rho_{11} = \rho_{22} = 1/2$ and $\rho_{33} = \rho_{44} = \rho_{43} = \rho_{34} = 0$. Hence the atomic coherences induced by the probe field can be expressed as

$$\rho_{41} = -\frac{\Omega_R}{2}\left[\frac{1+\frac{|\Omega_L|^2}{A}}{\Delta_{14} + \frac{|\Omega_c|^2}{\Delta_{13}^*} + \frac{|\Omega_L|^2}{\Delta_{12}^*}\left(1+\frac{|\Omega_R|^2}{A}\right)}\right], \tag{11a}$$

$$\rho_{42} = -\frac{\Omega_L}{2}\left[\frac{1-\frac{|\Omega_R|^2}{B}}{\Delta_{24} + \frac{|\Omega_c|^2}{\Delta_{23}^*} - \frac{|\Omega_R|^2}{\Delta_{12}}\left(1-\frac{|\Omega_L|^2}{B}\right)}\right]. \tag{11b}$$

The coefficients A and B are defined by

$$A = \Delta_{24}^*\Delta_{12}^*\left[1 - \left(\frac{|\Omega_R|^2}{\Delta_{24}^*\Delta_{12}^*} - \frac{|\Omega_c|^2}{\Delta_{24}^*\Delta_{23}}\right)\right], \tag{12a}$$

$$B = \Delta_{14}^*\Delta_{12}\left[1 + \left(\frac{|\Omega_L|^2}{\Delta_{14}^*\Delta_{12}} + \frac{|\Omega_c|^2}{\Delta_{14}^*\Delta_{13}}\right)\right]. \tag{12b}$$

The refractive indices for frequencies, $\omega_{R,L}$, can then be written in terms of the coherences given in Eq. (11) as

$$n_R = 1 + 2\pi\tilde{\eta}_R\mathrm{Re}\left[\frac{\rho_{41}}{\Omega_R}\right], \quad n_L = 1 + 2\pi\tilde{\eta}_L\mathrm{Re}\left[\frac{\rho_{42}}{\Omega_L}\right], \tag{13}$$

provided $\mathrm{Im}[\rho_{41(2)}/\Omega_{R(L)}] \sim 0$. The parameter $\tilde{\eta}_i = 3\mathcal{N}/2k_i^3$ $(i = R, L)$ is a dimensionless constant with $\mathcal{N}$ being the number of atoms per unit volume inside the medium.

C. Polarization rotation angle

The orthogonal polarization components of the VB behave differently while passing through an anisotropic medium. This property leads to the rotation of the polarization angle in the transverse plane. A brief derivation of the polarization rotation angle at each point on the VB's transverse plane is given below: the field envelopes of the two orthogonal polarization components of the VB can be written as

$$\mathcal{E}_L = \mathcal{E}_L^0\cos(\alpha)LG_0^{l_L}, \quad \mathcal{E}_R = \mathcal{E}_R^0 e^{i\theta}\sin(\alpha)LG_0^{l_R}, \tag{14}$$

where $\mathcal{E}_i^0$, α, and θ determine the field amplitudes, relative amplitude, and phase between the two modes, respectively, and $LG_0^{l_i}$ $(i = R, L)$ are the Laguerre Gaussian modes, with the radial index set to zero for simplicity:

$$LG_0^{l_i}(r,\phi,z) = E_i^{(0)}\sqrt{\frac{2}{\pi|l_i|!}}\left(\frac{r\sqrt{2}}{w(z)}\right)^{|l_i|}e^{-\frac{r^2}{w(z)^2}}e^{il_i\phi} \times \exp\left(\frac{ik_i^f n_i r^2 z}{2\left(z^2+n_i^2 z_R^2\right)}\right)e^{-i(|l_i|+1)\eta(z)+ik_i^f n_i z}. \tag{15}$$

In Eq. (15), l_i are the OAM index. The free space Rayleigh length is given by $z_R = k_i^f w_0^2/2$, where w_0 is the beam waist at $z = 0$ and k_i^f is the free space wave number. The beam radius at a propagation distance, z, inside the medium is given by $w(z) = w_0\sqrt{1 + z^2/n_i^2 z_R^2}$, where n_i is the refractive index of the medium for frequency, ω_i. The Gouy phase is given by $(|l_i|+1)\eta(z)$, with $\eta(z) = \tan^{-1}(z/n_i z_R)$. The azimuthal

and radial coordinates are denoted by ϕ and r, respectively. The output vector beam becomes elliptically polarized under the action of the anisotropic medium. Thus, to fully define the polarization state of the output field, one has to introduce the Stokes parameters. The Stokes parameters in the circular polarization basis are given by

$$S_0 = |\mathcal{E}_R|^2 + |\mathcal{E}_L|^2, \quad S_1 = 2\,\mathrm{Re}[\mathcal{E}_R^* \mathcal{E}_L],$$
$$S_2 = 2\,\mathrm{Im}[\mathcal{E}_R^* \mathcal{E}_L], \quad S_3 = |\mathcal{E}_R|^2 - |\mathcal{E}_L|^2. \tag{16}$$

The ellipticity, ζ, and orientation, ξ, of the polarization at each point on the VB's transverse plane can be calculated using

$$\frac{S_1}{S_0} = \cos(2\zeta)\cos(2\xi), \quad \frac{S_2}{S_0} = \cos(2\zeta)\sin(2\xi),$$
$$\frac{S_3}{S_0} = \sin(2\zeta). \tag{17}$$

From Eqs. (16) and (17), we get

$$\xi = \frac{1}{2}\tan^{-1}\left(\frac{S_2}{S_1}\right) = \frac{1}{2}\tan^{-1}\left(\frac{\mathrm{Im}[\mathcal{E}_R^* \mathcal{E}_L]}{\mathrm{Re}[\mathcal{E}_R^* \mathcal{E}_L]}\right). \tag{18}$$

For simplicity, the free space wave vectors for $\vec{E}_L$ and $\vec{E}_R$ are made equal, i.e., $\vec{k}_L^f = \vec{k}_R^f = \vec{k}^f$ (say). Substituting Eq. (14) and Eq. (15) in Eq. (18) gives

$$\xi(z) = -\frac{1}{2}\Bigg[\theta + \eta(z)\Delta(|l_{L,R}|) + \phi\Delta(l_{L,R}) + k^f z\Delta(n_{R,L}) + \frac{k^f z r^2}{2}\left\{\frac{n_R}{\left(z^2 + n_R^2 z_R^2\right)} - \frac{n_L}{\left(z^2 + n_L^2 z_R^2\right)}\right\}\Bigg], \tag{19}$$

where $\Delta|l_{L,R}| = |l_L| - |l_R|$, $\Delta(l_{L,R}) = l_L - l_R$, and $\Delta(n_{R,L}) = n_R - n_L$. Therefore, after propagating for a distance, z, the polarization at each point on the transverse plane of the VB rotates by an angle

$$\Delta\xi = \xi(z) - \xi(0) = -\frac{\Delta|l_{L,R}|\eta(z)}{2} - \left\{\frac{k^f z\Delta(n_{R,L})}{2} + \frac{k^f z r^2}{4}\left(\frac{n_R}{z^2 + n_R^2 z_r^2} - \frac{n_L}{z^2 + n_L^2 z_r^2}\right)\right\}. \tag{20}$$

In free space, $n_R = n_L = 1$, or any medium where $n_R = n_L$, Eq. (20) implies

$$\Delta\xi = -\tfrac{1}{2}\Delta|l_{L,R}|\eta(z). \tag{21}$$

From Eq. (21), if $|l_L| = |l_R|$ (e.g., for CV beams), there is no polarization rotation during free space propagation. For all other cases (such as FP beams) there will be a polarization rotation in accordance with Eq. (21) in free space or any medium where $n_R = n_L$.

D. Propagation equations

To investigate the effect of medium properties such as absorption, dispersion, diffraction, and anisotropicity on VB propagation, we study nonlinear Schrödinger equations under the slowly varying envelope and paraxial wave approximations. The beam propagation equations for the right and left circularly polarized components of the probe VB in terms of the respective Rabi frequencies are given as

$$\frac{\partial\Omega_R}{\partial z} = \frac{i}{2k_R}\nabla_\perp^2\Omega_R + \frac{2\pi i k_R \mathcal{N}|d_{14}|^2}{\hbar}\rho_{41}, \tag{22a}$$

$$\frac{\partial\Omega_L}{\partial z} = \frac{i}{2k_L}\nabla_\perp^2\Omega_L + \frac{2\pi i k_L \mathcal{N}|d_{24}|^2}{\hbar}\rho_{42}. \tag{22b}$$

The first terms on the right-hand side stand for the diffraction. The second terms on the right-hand side are responsible for the dispersion and absorption of both the components of probe VB. Note that the two propagation equations are coupled via the susceptibilities ρ_{41} and ρ_{42}. The propagation effect of the control field is neglected since the field is strong and undepleted throughout the length of propagation. Further, the envelope shape of the control field is considered to be diffraction-free Bessel Gaussian.

III. RESULTS

A. Polarization rotation control

The orthogonal components of VB must have different refractive indices to produce polarization rotation as stated in Eq. (20). The substantial contrast between n_R and n_L creates large polarization rotation. Hence the equal and opposite values of $n_{R,L}$ are the basic constraint for producing large polarization rotation. The variation of refractive index in the anisotropic medium is possible by changing the strength of the magnetic field. The difference in $n_{R,L}$ can be accomplished by making the probe VB's carrier frequency, ω_p, resonant with the intermediary state, $|0\rangle$, and excited state, $|4\rangle$, as shown in Fig. 1. With this configuration, the magnetic field, responsible for generating Zeeman sublevels, $|1\rangle$, $|0\rangle$, and $|2\rangle$, will red(blue) detune $\Omega_{R(L)}$ by an amount β_L. Due to the equal and opposite nature of detuning experienced by $\Omega_{R(L)}$, their medium responses with respect to β_L become laterally inverted mirror images of each other as shown in Figs. 2(a) and 2(b), respectively. Therefore, at any given value of β_L, $\mathrm{Re}[\chi_{41}] = -\mathrm{Re}[\chi_{42}]$, as apparent from Figs. 2(a) and 2(b). This makes $n_R \neq n_L$ according to Eq. (13), giving a

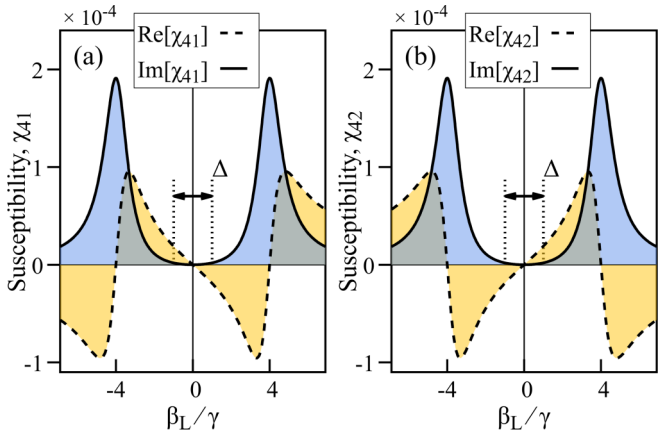

FIG. 2. (a), (b) Real and imaginary part of χ_{41} and χ_{42} vs β_L/γ, respectively. Parameters used: $\delta_p = \delta_c = 0$, $\Omega_{R,L} = 0.05\gamma$, $\Omega_c = 4\gamma$, $\Gamma_{ij} = 10^{-3}\gamma$, $\Gamma_{i4} \approx 3/2\gamma$ $(i < j;\ i, j = 1, 2, 3)$, and $\mathcal{N} = 2 \times 10^{11}$ cm^{-3}.

nonzero polarization rotation angle, coming from the curly bracketed term in Eq. (20). The Zeeman separation, β_L, is varied by changing $|\vec{B}|$ to change $\mathrm{Re}[\chi_{4i}]$, $(i \in 1, 2)$, as shown in Figs. 2(a) and 2(b), which in turn causes corresponding changes in $n_{R,L}$ according to Eq. (13). Moreover, the requirement of minimum absorption is fulfilled within the range of Δ as depicted in Fig. 2, thus enabling control of the polarization rotation angle via magnetic field with zero or minimum absorption.

B. Vector beam guiding

To guide the VB, the transverse spatial profile of the control beam is to be chosen in such a way that it creates a "core and cladding" type refractive index gradient for the components of VB. To form atomic waveguide structure, the control beam profile is taken to be a fundamental zeroth-order Bessel beam and is defined as

$$\Omega_c(r, \phi, 0) = \Omega_c^0 \mathcal{J}_0\Big(\frac{r}{w_0}\Big), \quad r = \sqrt{x^2 + y^2}. \tag{23}$$

The input amplitude of the Bessel control beam is denoted by Ω_c^0. The zeroth-order Bessel function of the first kind is denoted as $\mathcal{J}_0(r/w_0)$, where the full width half maximum of the central peak is approximately $2w_0^{-1}$. A Bessel beam undergoes diffractionless propagation inside the medium across several Rayleigh lengths (around $20z_R$) and it maintains the consistency of the refractive index gradient throughout. Thus the "core-cladding" type refractive index profile remains constant within that limited propagation length. The envelope shape of the control field is illustrated in Figs. 3(a) and 3(b). Figures 3(c) and 3(d) show the transverse refractive index profile of two orthogonal polarization components of the VB in the presence of a resonant control field, i.e., $\delta_c = 0$, at $\beta_L = 0.1\gamma$. On the other hand, Figs. 3(e) and 3(f) correspond to blue detuned control field $\delta_c = 0.2\gamma$ for the same β_L. In Figs. 3(c)–(f), there is a rise or fall in the refractive indices of $\Omega_{R,L}$, around the zeros of the Bessel control beam on the x axis. These refractive index extremums and the region between them serve as "cladding" and "core," respectively. For achieving waveguiding features, the core's refractive index needs to be higher than the cladding's, as displayed in Figs. 3(c), 3(e) and 3(f). Contrarily, there is no guiding when the core's refractive index is smaller than the cladding such as Fig. 3(d).

For control field detuning, $\delta_c = 0$, $\mathrm{Re}[\chi_{41}] = -\mathrm{Re}[\chi_{42}]$ at any given value of β_L within the EIT window, Δ, as shown in Figs. 2(a) and 2(b). In Figs. 2(a) and 2(c), for $\beta_L > 0$, $\mathrm{Re}[\chi_{41}] < 0$ and $\mathrm{Re}[\chi_{42}] > 0$, which makes $n_R < 1$ and $n_L > 1$, in accordance with Eq. (13). This is reflected in Figs. 3(c) and 3(d), where, for $\beta_L = 0.1\gamma > 0$ at $\delta_c = 0$, the transverse profiles of refractive indices, $\mathrm{Re}[n_{R,L}]$, are inverted images of each other. Figures 3(c) and 3(d) suggest that the right circularly polarized component, Ω_R, will be guided, while the left circularly polarized component, Ω_L, will undergo diffraction. Thus, for simultaneous waveguiding of $\Omega_{R,L}$, both $n_{R,L}$ must be less than unity for a given value of β_L and δ_c. This can be achieved by considering a blue detuned control field, $\delta_c > 0$. For example, in Fig. 4, at $\delta_c = 2\gamma$, the zero point (marked with small circles) of $\mathrm{Re}[\chi_{41}]$ and $\mathrm{Re}[\chi_{42}]$, within the EIT

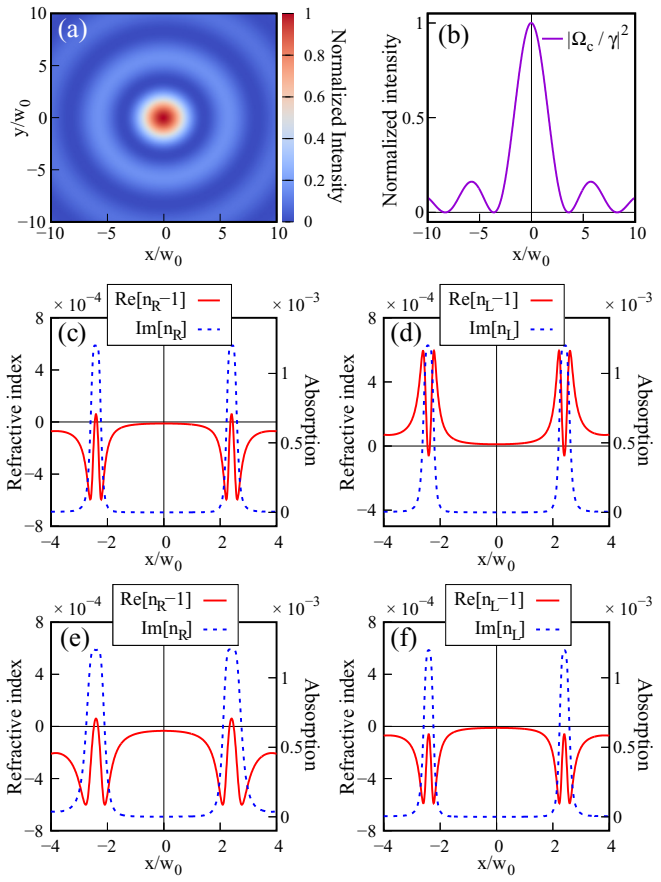

FIG. 3. (a), (b) Transverse intensity profile of control field. In Figs. (c)– (f), "solid line": transverse profile of $\mathrm{Re}[n_i - 1]$ $(i = R, L)$; "dotted line": transverse profile of $\mathrm{Im}[n_i]$ (absorption). For all the plots, $\delta_p = 0$, $\beta_L = 0.1\gamma$. Plots (c) and (d) are generated with $\delta_c = 0$, while plots (e) and (f), with $\delta_c = 0.2\gamma$. Other parameters used remain the same as mentioned in Fig. 2.

window, are shifted leftwards and rightwards, respectively, by 2γ. As a result, within $-2\gamma < \beta_L < 2\gamma$, both $\mathrm{Re}[\chi_{41}] < 0$ and $\mathrm{Re}[\chi_{42}] < 0$, which implies, $n_{R,L} < 1$. Thus, in general, $\delta_c > 0$ and $-\delta_c < \beta_L < \delta_c$ generates the desired "core-cladding" refractive index profile for both $\Omega_{R,L}$ as shown in Figs. 3(e) and 3(f), which were plotted by taking $\delta_c = 0.2\gamma > 0$ and $-0.2\gamma < \beta_L = 0.1\gamma < 0.2\gamma$. Again, in Fig. 4, for $\delta_c > 0$ and $-\delta_c < \beta_L < \delta_c$, the susceptibilities of $\Omega_{R,L}$ are unequal, i.e., $n_R \neq n_L$. This results in a polarization rotation of the VB during propagation in accordance with Eq. (20). With the above parameter constraint in mind, the propagation results for a CV beam are curated in Fig. 5. Figures 5(a) and 5(b) are the transverse polarization distribution of a CV beam at $z = 0$ and $z = 2z_R$, respectively. In Fig. 5(b) the polarization ellipses at each point on the VB's transverse plane has rotated by a certain angle and its polarization state has changed from radial to azimuthal. With increasing propagation length, the azimuthal distribution will change to spiral and then back to radial in a cyclic manner along the propagation length. This sort of rotation is not observed for CV beams during free space propagation [Eq. (21)] and is a consequence of the magnetic-field-induced anisotropy. Figure 5(c) shows a comparison between the one-dimensional transverse profile of

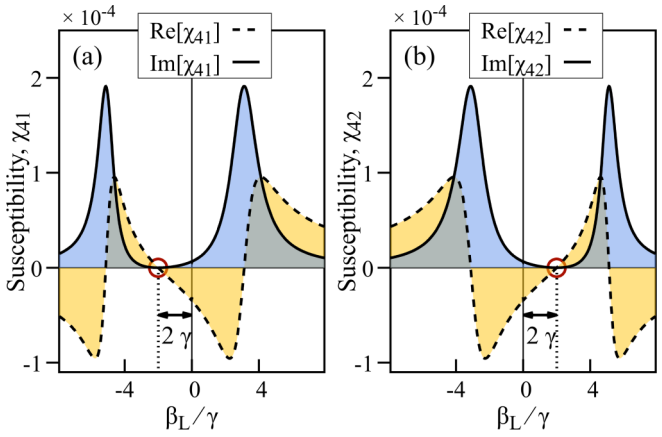

FIG. 4. (a), (b) Real and imaginary part of χ_{41} and χ_{42} vs β_L/γ, respectively, with $\delta_p = 0$ and $\delta_c = 2\gamma$. Other parameters used remain the same as mentioned in Fig. 2. The small circular markings in (a) and (b) indicate the zero point of Re$[\chi_{4i}]$ within the EIT window.

$\Omega_{R,L}$ at a given propagation length. In Fig. 5(c), the degree of waveguiding for $\Omega_{R,L}$ is slightly different. This is because, within the requisite parameter region for waveguiding, $\delta_c > 0$, $-\delta_c < \beta_L < \delta_c$, the susceptibilities of $\Omega_{R,L}$ are not equal as seen in Fig. 4. Figure 5(d) shows the longitudinal profile of

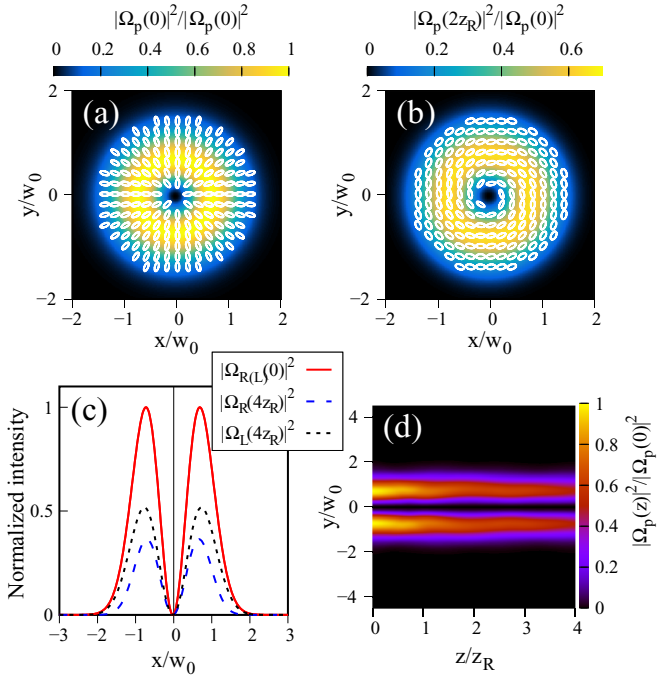

FIG. 5. (a), (b) Transverse intensity and polarization distribution of a CV beam ($l_L = -1$, $l_R = 1$, $\theta = 0$, $\alpha = \pi/8$) at $z = 0$ and $z = 2z_R$, respectively. (c) Normalized intensity vs x/w_0. (d) Longitudinal intensity profile of the VB. Control field beam waist is taken to be $1.4w_0$, where w_0 is the beam waist of the probe VB. The white color ellipses in (a) and (b) represent left circular polarization. Parameters used: $\delta_c = 0.2\gamma$, $\beta_L = 0.05\gamma$, with the rest of the parameters the same as Fig. 2. Field amplitudes have been normalized with respect to the field amplitude at $z = 0$.

the CV beam. In Fig. 5(d), the CV beam is smoothly guided up to four Rayleigh lengths, beyond which the VB's intensity noticeably depletes. This is a consequence of the cumulative absorption at the core-cladding boundary [see Figs. 3(e) and 3(f)] during propagation. In the next section, we shall discuss the factors responsible for smooth waveguiding.

C. Effect of control beam waist

In this section, we discuss how the Bessel control beam's width dictates the guiding of the VB through atomic vapor. The sizes of the Bessel control beam's central lobe and the core of the optically written waveguide are approximately the same. The core's radius can be changed by varying the control beam size. Figure 6 shows the longitudinal profiles of a CV beam for different control beam waists. In Figs. 6(a) and 6(b), control beam waists are $0.5w_0$ and w_0, respectively. The CV beam exhibits an oscillatory longitudinal variation, closely resembling that of an actual optical fiber. In Fig. 6(c), for a control beam waist of $1.4w_0$, the CV beam experiences a smooth guiding. Increasing the control beam waist to $2w_0$ as shown in Fig. 6(d), the oscillatory behavior reappears with a larger period compared to Figs. 6(a) and 6(b). The explanation for Fig. 6(d) is as follows: here the Bessel-control beam waist at the medium entrance is $2w_0$, which creates a core of approximately the same radii, $2w_0$. Therefore, a probe CV beam of waist w_0 would undergo broadening due to diffraction until its beam waist becomes equal to the core's radius, i.e., $2w_0$. Subsequently, the CV beam would be guided back towards the core's axis due to total internal reflection at the core-cladding boundary. Since the core is a nonabsorbing or diffracting media (free space like) as seen in Figs. 3(c)–3(f), the CV beam would have to propagate approximately two Rayleigh lengths to have a broadened beam waist of $\approx 2w_0$. This is because the beam waist of an LG beam after free space propagation of two Rayleigh lengths is $\sqrt{5}w_0$, which can be rounded off to $2w_0$. Thus the CV beam expands and contracts at an interval of two Rayleigh lengths along the longitudinal direction as seen in Fig. 6(d). In Fig. 6(d), the dotted lines, "$y/w_0 = -2$" and "$z/z_R = 2$," represent the core boundary and position of two Rayleigh length on z axis, respectively. The intersection point of these two lines is where the CV beam is reflected inside the core via total internal reflection. The expansion and contraction observed in Figs. 6(a) and 6(b) for control beam waists $0.5w_0$ and w_0, respectively, is of the same nature as Fig. 6(d). In Fig. 6(a), the CV beam undergoes rapid compression near the medium entrance due to the core's size being smaller than VB's spot size. After this, the VB undergoes the aforementioned oscillatory longitudinal variation. Same explanation applies to the case in Fig. 6(b). In Fig. 6(c), the control beam waist is $1.4w_0$ ($\approx\sqrt{2}w_0$), which is approximately the beam waist of an LG beam after free space propagation of one Rayleigh length. Therefore, the CV beam broadens to about $1.4w_0$ at one Rayleigh length, before undergoing total internal reflection at the core-cladding boundary. The expansion of the CVB from w_0 to $1.4w_0$ is very small and thus results in a smooth guiding. Therefore, to achieve smooth waveguiding, the control beam waist has to lie within a range of approximately $[1.2w_0, 1.6w_0]$.

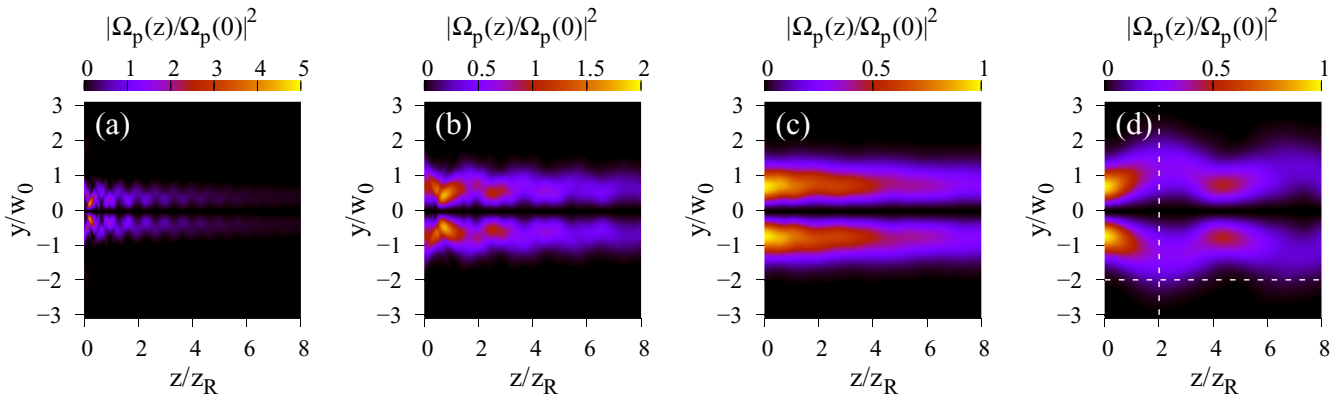

FIG. 6. (a)–(d) Longitudinal intensity profile of a CV beam ($l_L = -1$, $l_R = 1$, $\theta = 0$, $\alpha = \pi/8$) for control field beam waists $0.5w_0$, w_0, $1.4w_0$, and $2w_0$, respectively. Parameters used: $\delta_c = 0.2\gamma$, $\beta_L = 0.05\gamma$. All other parameters and field amplitude normalization remains the same as Fig. 5.

IV. CONCLUSION

In conclusion, we theoretically investigated a vector beam guiding scheme through an atomic vapor medium, with a four-level tripod system. The three transitions of the four-level tripod system are coupled by a strong zeroth-order Bessel control beam and the two orthogonally polarized components of a weak vector beam, in the presence of an external longitudinal magnetic field. With appropriate parameters, the spatial intensity profile of the control beam can create a core and cladding type refractive index gradient along the radial direction from the beam propagation axis. Due to the nondiffractive property of a Bessel beam, the "core-cladding" created by it remains unchanged across its diffractionless propagation length. We have shown that a weak vector beam of slightly smaller diameter than the core is guided through the medium for several Rayleigh lengths. In addition to waveguiding, the magnetic-field-induced anisotropy in the four-level tripod system creates a difference in the refractive indices of the vector beam's two orthogonal polarization components. This results in polarization rotation of cylindrical vector beams (CVBs) which are otherwise polarization invariant under free-space propagation. Thus creating diffractionless CVBs with polarization gradient across the propagation length, e.g., a radial CVB, would change to azimuthal, then to spiral, and back to radial in a periodic manner along the propagation length. Due to the higher focusability of radial over azimuthal CVBs, the ability to change the polarization state of a CVB may be useful in achieving a variable degree of focusing. Furthermore, the vector beam can be squeezed as desired by reducing the control beam's radius. Therefore, as a proof of concept, the proposed scheme can guide a weak vector beam, whilst enabling control over its polarization rotation. Our work may also have applications in polarization-based measurements with vector beams, increasing optical density of a medium, etc., where vector beam focusing, guiding, and polarization rotation control might be simultaneously desired.

ACKNOWLEDGMENTS

N.D. and T.N.D. gratefully acknowledge funding by the Science and Engineering Board (Grant No. CRG/2018/000054). P.K. acknowledges the financial support from the Max Planck Society.

APPENDIX: EFFECT OF INHOMOGENEOUS BROADENING

In this Appendix, we discuss the effect of inhomogeneous broadening on the proposed VB guiding scheme. The Doppler effect causes a laser frequency shift in the atom's rest frame, introducing a laser detuning, $\tilde{\delta}_i(\vec{v}) = \delta_i + \vec{k}_i.\vec{v}$ $[i = p, c]$, that is dependent on the velocity, $\vec{v}$, of the atom. Here, $\vec{k}_i$ is the wave vector of the laser field. With the aforementioned modified detuning, the steady-state susceptibility, χ_{ij}, are given by their average over the one-dimensional Maxwell-Boltzmann velocity distribution:

$$f(v)dv = \sqrt{\frac{M}{2\pi k_B T}} \exp\left(-\frac{Mv^2}{2k_B T}\right)dv, \qquad \text{(A1)}$$

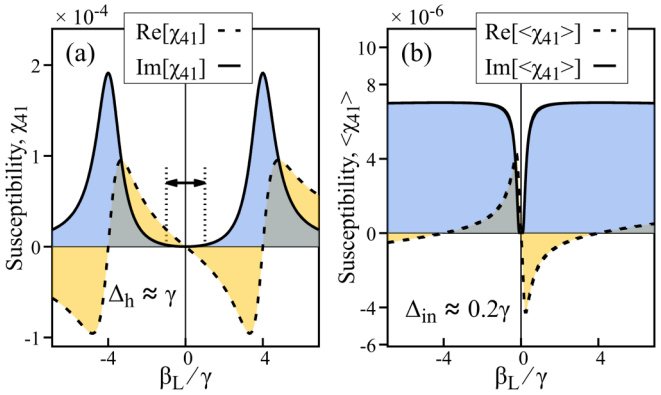

FIG. 7. (a), (b) Real and imaginary part of homogeneously broadened susceptibility, χ_{41}, and Doppler averaged susceptibility, $\langle\chi_{41}\rangle$ vs β_L/γ, respectively. Parameters used: Rabi frequencies, $\Omega_c = 4\gamma$, $\Omega_{R(L)} = 0.05\gamma$; detunings, $\delta_{p(c)} = 0$; decoherence rates, $\Gamma_{ij} \approx 10^{-3}\gamma$, $\Gamma_{i4} = 3/2\gamma$ $(i < j,\ i, j = 1, 2, 3)$; density of atoms, $\mathcal{N} = 2 \times 10^{11}$ cm^{-3}; temperature $T = 300$ K. Here, Δ_h and Δ_{in} represent the width of the EIT window for homogeneous and inhomogeneous broadening, respectively.

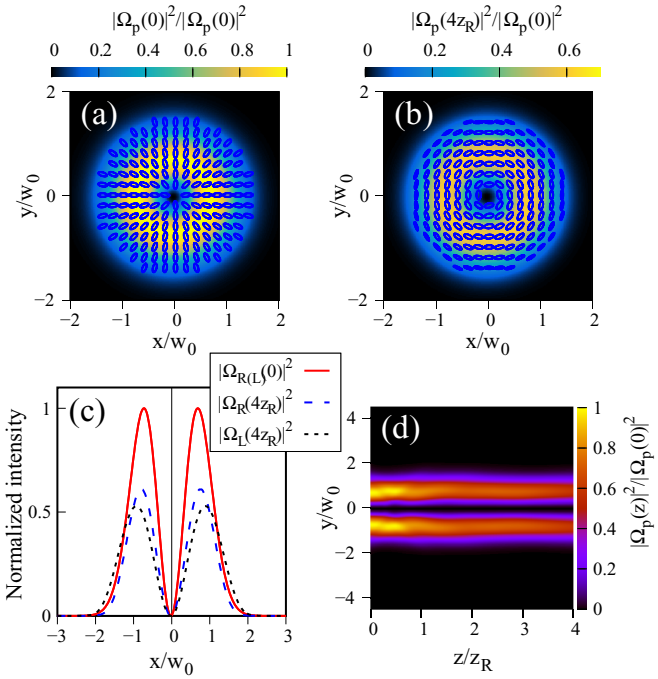

FIG. 8. (a), (b) Transverse intensity and polarization distribution of a CV beam ($l_L = -1$, $l_R = 1$, $\theta = 0$, $\alpha = 3\pi/8$) at $z = 0$ and $z = 4z_R$, respectively. (c) Normalized intensity vs x/w_0. (d) Longitudinal intensity profile of the VB. Control field beam waist is taken to be w_0. The blue color ellipses in (a) and (b) represent right circular polarization. Parameters used: $\delta_c = 0.1\gamma$, $\delta_p = 0$, $\beta_L = 0.05\gamma$, and $\Omega_c = 8\gamma$ with the rest of the parameters the same as Fig. 7.

where T is the temperature of the gas, M is the mass of each atom, and k_B is the Boltzmann constant. The velocity averaged susceptibilities are then given by $\langle \chi_{ij} \rangle = \int_{-\infty}^{\infty} \chi_{ij}(v) f(v) dv$.

We consider a copropagating geometry, with both probe and control fields propagating along the $+z$ direction, i.e., $\vec{k}_p/|\vec{k}_p| = \vec{k}_c/|\vec{k}_c| = \hat{z}$. Furthermore, for simplicity of our calculations, we considered the wave numbers for both control and probe fields to be the same, i.e., $|\vec{k}_p| \approx |\vec{k}_c|$. As a result the two-photon detuning in the presence of inhomogeneous broadening becomes

$$\begin{aligned} \tilde{\delta}(\vec{v}) &= \tilde{\delta}_p(\vec{v}) - \tilde{\delta}_c(\vec{v}) \\ &= \delta_p + \vec{k}_p \cdot \vec{v} - (\delta_c + \vec{k}_c \cdot \vec{v}) \\ &\approx \delta_p - \delta_c, \end{aligned} \tag{A2}$$

which is the same as the two-photon detuning for homogeneous broadening. Thus the copropagating geometry is preferable to reduce the effect of inhomogeneous broadening. In Figs. 7(a) and 7(b), the real and imaginary parts of susceptibility, corresponding to the VB's right circularly polarized component for homogeneous and inhomogeneous broadening, are respectively plotted. In the case of inhomogeneous broadening, the width of the EIT window ($\Delta_{\text{in}} \approx 0.2\gamma$) shrinks as shown in Fig. 7(b). Furthermore, the magnitude of susceptibility for inhomogeneous broadening is comparatively smaller than homogeneous broadening as shown in Figs. 7(a) and 7(b). Due to a very narrow EIT window in the case of inhomogeneous broadening, the control field Rabi frequency needs to be larger, say $\Omega_c = 8\gamma$, compared to $\Omega_c = 4\gamma$ as mentioned in Fig. 5, to increase the EIT window width. The strengthening of the control field intensity leads to an absorption free VB guiding through the core of the optically written waveguide. The propagation results obtained by considering inhomogeneous broadening are curated in Fig. 8. The results suggest that VB guiding should also be possible in the presence of inhomogeneous broadening by choosing a larger value of control field Rabi frequency, as illustrated in the figure. Therefore, the proposed VB guiding scheme should be experimentally feasible for both warm [31] as well as ultracold [32] rubidium atomic vapor.

[1] Q. Zhan, Adv. Opt. Photon. **1**, 1 (2009).
[2] A. M. Beckley, T. G. Brown, and M. A. Alonso, Opt. Express **18**, 10777 (2010).
[3] E. J. Galvez, S. Khadka, W. H. Schubert, and S. Nomoto, Appl. Opt. **51**, 2925 (2012).
[4] A. M. Yao and M. J. Padgett, Adv. Opt. Photon. **3**, 161 (2011).
[5] R. Dorn, S. Quabis, and G. Leuchs, Phys. Rev. Lett. **91**, 233901 (2003).
[6] B. Hao and J. Leger, Opt. Express **15**, 3550 (2007).
[7] T. A. Klar and S. W. Hell, Opt. Lett. **24**, 954 (1999).
[8] P. Török and P. Munro, Opt. Express **12**, 3605 (2004).
[9] K. S. Youngworth and T. G. Brown, Opt. Express **7**, 77 (2000).
[10] S. N. Khonina and I. Golub, J. Opt. Soc. Am. A **29**, 1470 (2012).
[11] V. G. Niziev and A. V. Nesterov, J. Phys. D **32**, 1455 (1999).
[12] Q. Zhan, J. Opt. A: Pure Appl. Opt. **5**, 229 (2003).
[13] Q. Zhan, Trapping nanoparticles with cylindrical polarization, in *Optical Trapping and Optical Micromanipulation*, Vol. 5514, edited by K. Dholakia and G. C. Spalding, International Society for Optics and Photonics (SPIE, 2004), pp. 275–282.
[14] F. K. Fatemi, Opt. Express **19**, 25143 (2011).
[15] V. Parigi, V. D'Ambrosio, C. Arnold, L. Marrucci, F. Sciarrino, and J. Laurat, Nat. Commun. **6**, 7706 (2015).
[16] C. Gabriel, A. Aiello, W. Zhong, T. G. Euser, N. Y. Joly, P. Banzer, M. Förtsch, D. Elser, U. L. Andersen, C. Marquardt, P. S. J. Russell, and G. Leuchs, Phys. Rev. Lett. **106**, 060502 (2011).
[17] G. Milione, M. P. J. Lavery, H. Huang, Y. Ren, G. Xie, T. A. Nguyen, E. Karimi, L. Marrucci, D. A. Nolan, R. R. Alfano, and A. E. Willner, Opt. Lett. **40**, 1980 (2015).
[18] G. Milione, H. I. Sztul, D. A. Nolan, and R. R. Alfano, Phys. Rev. Lett. **107**, 053601 (2011).
[19] G. Agrawal, *Nonlinear Fiber Optics*, 5th ed. (Academic Press, Boston, 2013).
[20] W. J. Firth and D. V. Skryabin, Phys. Rev. Lett. **79**, 2450 (1997).
[21] A. S. Desyatnikov and Y. S. Kivshar, Phys. Rev. Lett. **87**, 033901 (2001).
[22] Z.-H. Zhu, P. Chen, H.-W. Li, B. Zhao, Z.-Y. Zhou, W. Hu, W. Gao, Y.-Q. Lu, and B.-S. Shi, Appl. Phys. Lett. **112**, 161103 (2018).

[23] M. S. Bigelow, P. Zerom, and R. W. Boyd, Phys. Rev. Lett. **92**, 083902 (2004).
[24] Y. V. Izdebskaya, J. Rebling, A. S. Desyatnikov, and Y. S. Kivshar, Opt. Lett. **37**, 767 (2012).
[25] F. Bouchard, H. Larocque, A. M. Yao, C. Travis, I. De Leon, A. Rubano, E. Karimi, G.-L. Oppo, and R. W. Boyd, Phys. Rev. Lett. **117**, 233903 (2016).
[26] C. J. Gibson, P. Bevington, G.-L. Oppo, and A. M. Yao, Phys. Rev. A **97**, 033832 (2018).
[27] A. G. Truscott, M. E. J. Friese, N. R. Heckenberg, and H. Rubinsztein-Dunlop, Phys. Rev. Lett. **82**, 1438 (1999).
[28] S. Sharma and T. N. Dey, Phys. Rev. A **96**, 053813 (2017).
[29] C. Guo, S. Fu, H. Lin, Z. Li, H. Yin, and Z. Chen, Opt. Express **26**, 18721 (2018).
[30] I. Moreno, J. A. Davis, M. M. Sánchez-López, K. Badham, and D. M. Cottrell, Opt. Lett. **40**, 5451 (2015).
[31] M. M. Kash, V. A. Sautenkov, A. S. Zibrov, L. Hollberg, G. R. Welch, M. D. Lukin, Y. Rostovtsev, E. S. Fry, and M. O. Scully, Phys. Rev. Lett. **82**, 5229 (1999).
[32] F. Castellucci, T. W. Clark, A. Selyem, J. Wang, and S. Franke-Arnold, Phys. Rev. Lett. **127**, 233202 (2021).